Orientational Ordering in Athermally Sheared, Aspherical, Frictionless Particles Supplemental Material

Theodore Marschall,[1] Yann-Edwin Keta,[2,3,4] Peter Olsson,[2] and S. Teitel[1]

[1] *Department of Physics and Astronomy, University of Rochester, Rochester, NY 14627*
[2] *Department of Physics, Umeå University, 901 87 Umeå, Sweden*
[3] *Département de Physique, École Normale Supérieure de Lyon, 69364 Lyon Cedex 07, France*
[4] *Département de Physique, Université Claude Bernard Lyon 1, 69622 Villeurbanne Cedex, France*

(Dated: March 13, 2019)

In this Supplemental Material we provide further details and tests to demonstrate the correctness of our simulations. In Sec. I we demonstrate the validity of our results for the nematic order parameter S_2 at our smallest asphericity, $\alpha = 0.001$, which is key to our conclusion that $S_{2\,\max}$ stays finite as $\alpha \to 0$. In Sec. II we discuss translational correlations in our system and demonstrate that there is no smectic ordering into well defined flowing layers. In Sec. III we show that the onset for the effect that particle contacts to prefer to lie on the narrowest width of the particles, takes place as the packing ϕ increases through the jamming transition. In Sec. IV we consider the effect of a pure shear deformation on 2D spherocylinders, and contrast with our main results for simple shear. In Sec. V we provide details on how we determine when two particles are in contact, and compute the corresponding overlap parameters.

I. VALIDITY OF RESULTS AT $\alpha = 0.001$

Our argument in the main text, that $\lim_{\alpha\to 0}[S_{2\,\max}] = S_0$ is finite, relied on the assertion that our data at the smallest $\alpha = 0.001$ are reliable. In order to argue conversely, i.e., that $S_{2\,\max}$ vanishes as a power law as $\alpha \to 0$, we would have to believe that the value of $S_{2\,\max}$ at $\alpha = 0.001$ that is reported in Fig. 4a of the main text is, by some artifact of our simulations, larger than it should be.

Here we provide several tests to support our claim that our data point at $\alpha = 0.001$ is indeed correct. Since our simulations for 2D spherocylinders are considerably less time consuming than for 3D ellipsoids, we can make more exacting tests for that case. Hence, here we restrict ourselves to 2D spherocylinders.

A. Dependence on Shear Strain Rate

As shown in Fig. 1 of the main text, the nematic order parameter S_2 depends on both packing fraction ϕ and shear strain rate $\dot\gamma$. However at each ϕ, S_2 approaches a limiting value as $\dot\gamma$ decreases. Here we wish to confirm that we have simulated at small enough $\dot\gamma$ so that the peak value $S_{2\,\max}$ which we find for $\alpha = 0.001$ has reached this $\dot\gamma \to 0$ limit. In Fig. SM-1a we plot S_2 vs ϕ for our three smallest strain rates $\dot\gamma$, using a system with $N = 1024$ particles. Just as was found in Fig. 1 of the main text for a larger α, here we see $\dot\gamma$ dependence remaining on the large ϕ side of the peak in S_2, however there is no $\dot\gamma$ dependence on the low ϕ side up to, and including, the peak value. Thus our results of Fig. SM-1a clearly argue that the value of $S_{2\,\max}$ will not decrease if $\dot\gamma$ were made even smaller.

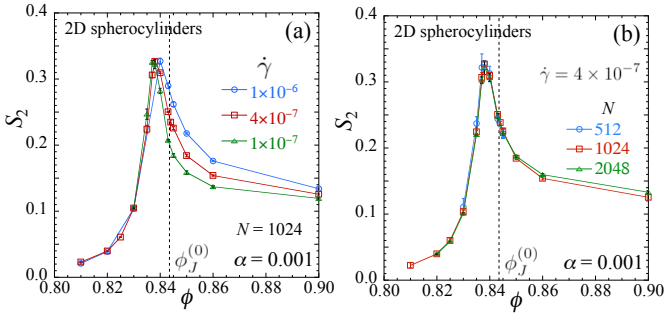

FIG. SM-1. Nematic order parameter S_2 for $\alpha = 0.001$ vs packing fraction ϕ for (a) three different shear strain rates $\dot\gamma$ with $N = 1024$ particles, and (b) systems with different numbers of particles N for $\dot\gamma = 4\times10^{-7}$. Vertical dashed lines locate the jamming transition of $\alpha = 0$ spherical particles, $\phi_J^{(0)} = 0.8433$.

B. Dependence on System Size

As one approaches the jamming transition, a correlation length diverges. If one is too close to the jamming transition, finite size effects may become important when the correlation length becomes larger than the length of the system. We thus wish to check that our value of $S_{2\,\max}$ for $\alpha = 0.001$ is not affected by such possible finite system size effects. Our results in the main text are for systems with $N = 1024$ particles. In Fig. SM-1b we plot S_2 vs ϕ at the small strain rate $\dot\gamma = 4 \times 10^{-7}$, using three different systems sizes with numbers of particles $N = 512, 1024$ and 2048. While there is a small dependence on N seen at the largest ϕ, there is no dependence on N at lower ϕ up to and including the peak value. Our value of $S_{2\,\max}$ for $\alpha = 0.001$ thus does not suffer from finite size effects.

C. Dependence on Integration Time Step

We should also check if there is any dependence of our results on the size of the finite numerical integration step Δt. Our results in the main text used a value $\Delta t = 0.02 t_0$ with $t_0 = D_s^2 k_d / k_e$ the unit of time. In Fig. SM-2 we plot S_2 vs ϕ at the small strain rate $\dot\gamma = 4 \times 10^{-7}$, for $\alpha = 0.001$, using three different values of the time step $\Delta t/t_0 = 0.01, 0.02$ and 0.04. We see that any differences between the data from the three different Δt are within the estimated statistical error. We conclude that our integration step of $\Delta t/t_0 = 0.02$ is small enough to accurately determine $S_{2\,\max}$ for $\alpha = 0.001$.

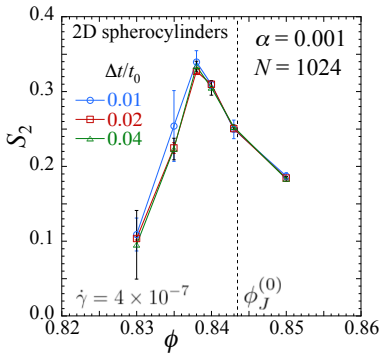

FIG. SM-2. Nematic order parameter S_2 for $\alpha = 0.001$ vs packing fraction ϕ using different integration time steps $\Delta t/t_0 = 0.01, 0.02$ and 0.04. The system is sheared at a strain rate $\dot\gamma = 4 \times 10^{-7}$ and has $N = 1024$ particles. Vertical dashed line locates the jamming transition of $\alpha = 0$ spherical particles, $\phi_J^{(0)} = 0.8433$.

D. Equilibration

Finally we demonstrate that the rotational degrees of freedom in our system are well equilibrated for our simulations at $\alpha = 0.001$. When α is small, the small moment arms of the collisional forces result in small torques, and, depending on the particle density, it can require long shear strains for the rotational degrees of freedom of the system to equilibrate to the proper steady state.

Let us define $S_2(\gamma)$ as the magnitude of the instantaneous nematic order parameter of the individual configuration of the system after it has sheared a strain $\gamma = \dot\gamma t$. For an initial configuration of randomly oriented particles, a system with a finite number of particles N will have some initial value $S_2(0)$. At low densities, where torque inducing collisions are rare, particles will rotate primarily under the influence of the dissipative torque. In this case, since particles with finite α have a non uniform angular velocity that depends on their orientation θ_i, the relative orientations of the particle spines $\hat{\boldsymbol{\ell}}_i$ will vary with γ and hence so will S_2. But once the system has strained so that $\gamma = \dot\gamma T$, where T is the period of rotation of an isolated particle, the particles will have returned to their initial orientations and $S_2(\gamma)$ will have returned to its initial value $S_2(0)$. We thus expect to see an oscillating $S_2(\gamma)$ with period $\dot\gamma T$. We have observed such behavior for small α at low densities. However, as the density increases the rate of collisions increases. These collisions will perturb this oscillatory behavior until, after a sufficiently large strain has been applied, the particle orientations have lost memory of their initial configuration. The particle orientations will then sample a stationary steady state distribution. $S_2(\gamma)$ will then be constant, aside from random fluctuations that we might expect should decrease as $1/\sqrt{N}$ as the number of particles N increases.

In Fig. SM-3a we plot $S_2(\gamma)$ vs γ for a shear strain rate $\dot\gamma = 4 \times 10^{-7}$ at a packing $\phi = 0.838$ near the peak in S_2, for a system with $N = 1024$ particles with $\alpha = 0.001$. We see that $S_2(\gamma)$ appears, as desired, to consist of random fluctuations about a constant average. The dashed horizontal line in Fig. SM-3a is the average $\langle S_2(\gamma)\rangle = (1/\Delta\gamma)\int_{\gamma_i}^{\gamma_f} d\gamma\, S_2(\gamma)$, where $\Delta\gamma = \gamma_f - \gamma_i$; we start averaging only after an initial shear strain of $\gamma_i = 10$ so as to avoid any initial transients, and average up to a final $\gamma_f = 150$. The solid horizontal line represents the ensemble average S_2, as considered elsewhere in this work. To be clear, $S_2(\gamma)$ is the largest eigenvalue of the orientational ordering tensor $T_{\mu\nu}(\gamma)$ as computed for the individual configuration at strain γ, while S_2 is the largest eigenvalue of the orientational ordering tensor $\langle T_{\mu\nu}\rangle$ averaged over the length of the shearing run from γ_1 to γ_2. Since the relation between eigenvalue and tensor is not linear, these two averages of S_2 need not be equal, and in Fig. SM-3a we see that there is indeed a small difference. Since the direction of the nematic director is optimized to give the largest possible S_2, and since the direction of the nematic director obtained from $T_{\mu\nu}(\gamma)$ fluctuates as γ varies from configuration to configuration (as opposed to the director obtained from $\langle T_{\mu\nu}\rangle$ which is fixed), we expect that $\langle S_2(\gamma)\rangle$ will be somewhat larger than S_2, and this is indeed what is observed in Fig. SM-3a. In Fig. SM-3b we plot $\langle S_2(\gamma)\rangle - S_2$ vs N and see that this difference is going to zero as N increases. In the same figure we also plot the standard deviation $\sigma_{S_2(\gamma)} = \sqrt{\langle S_2^2(\gamma)\rangle - \langle S_2(\gamma)\rangle^2}$ vs N and see that it also vanishes as N increases.

Next, we consider the Fourier transform of $S_2(\gamma)$ in order to check that the frequency spectrum of the fluctuating noise seen in Fig. SM-3a is broad without any peaks that could indicate vestigial oscillations due to poor equilibration. Since $S_2(\gamma)$ is plotted in terms of the dimensionless time $\gamma = \dot\gamma t$, in Fig. SM-4 we plot the Fourier transform $\mathcal{F}[S_2]$ as a function of the dimensionless frequency $\omega/\dot\gamma$. We see that the spectrum is indeed broad with no peaks. The high frequency tail is roughly power law with an exponent 1.3, however that exponent changes a bit depending on the range of γ that is used in the fit.

Lastly we consider a similar analysis of the orientation

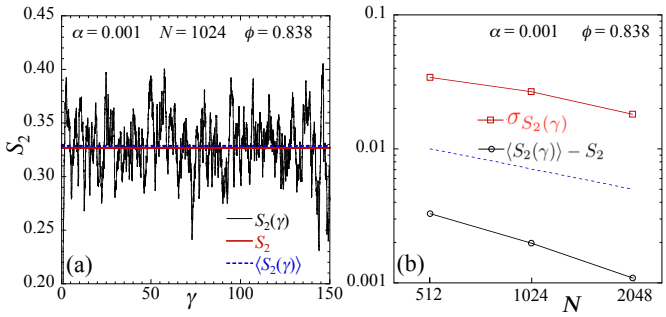

FIG. SM-3. (a) Instantaneous nematic order parameter $S_2(\gamma)$ vs shear strain γ, for $\alpha = 0.001$ and shear strain rate $\dot{\gamma} = 4 \times 10^{-7}$ at packing fraction $\phi = 0.838$ near the peak value $S_{2\,\max}$. The horizontal dashed line is the average over these instantaneous values $\langle S_2(\gamma)\rangle$, while the horizontal solid line is S_2 as obtained from averaging the orientational ordering tensor over the entire shearing run. The system has $N = 1024$ particles. (b) Difference $\langle S_2(\gamma)\rangle - S_2$ vs number of particles N, and standard deviation $\sigma_{S_2(\gamma)}$ vs N; the dashed line is $\sim 1/\sqrt{N}$ for comparison.

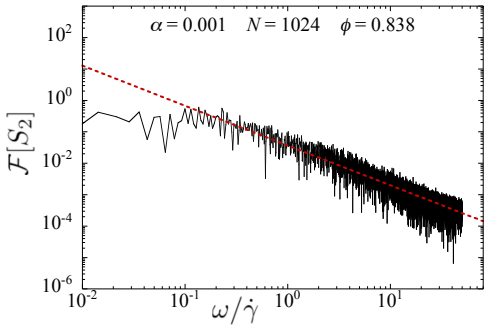

FIG. SM-4. Fourier transform of $S_2(\gamma)$, $\mathcal{F}[S_2]$, vs dimensionless frequency $\omega/\dot{\gamma}$. The high frequency tail is fit to an inverse power law (dashed line) and gives an exponent ~ 1.3.

angle θ_2 of the nematic director. In Fig. SM-5a we plot the instantaneous $\theta_2(\gamma)$ vs γ for the same parameters as in Fig. SM-3a, $\dot{\gamma} = 4 \times 10^{-7}$, $\phi = 0.838$, $\alpha = 0.001$. We see what appear to be random fluctuations about a constant average value. The dashed horizontal line is the average $\langle\theta_2(\gamma)\rangle = (1/\Delta\gamma)\int_{\gamma_i}^{\gamma_f} d\gamma\,\theta_2(\gamma)$, while the solid horizontal line is θ_2 obtained from the ensemble averaged orientation tensor $\langle T_{\mu\nu}\rangle$. In Fig. SM-5b we plot the Fourier transform $\mathcal{F}[\theta_2]$ vs the dimensionless frequency $\omega/\dot{\gamma}$. We see a broad spectrum with a power law tail decreasing with an exponent ~ 1.5 (the exact value of this exponent is sensitive to the range of data used in the fit). There are no peaks in $\mathcal{F}[\theta_2]$ to indicate any oscillatory motion, thus giving support to the assertion in the main text that, while individual particles tumble with an average angular velocity $\langle\omega_i\rangle$, there is no coherent tumbling of the nematic order parameter $\mathbf{S}_2$. Our results in this section thus confirm that our spherocylinder simulations at $\alpha = 0.001$ are indeed well equilibrated.

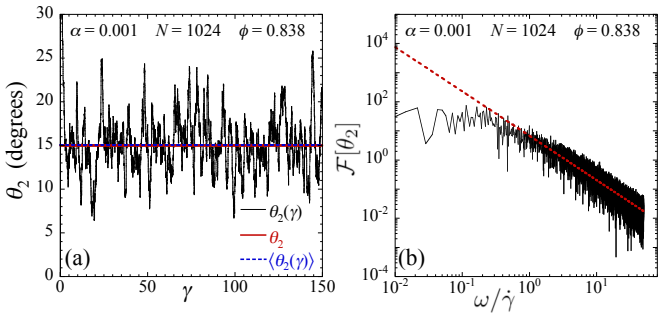

FIG. SM-5. (a) Instantaneous nematic director angle $\theta_2(\gamma)$ vs shear strain γ, for $\alpha = 0.001$ and shear strain rate $\dot{\gamma} = 4\times10^{-7}$ at packing fraction $\phi = 0.838$ near the peak value $S_{2\,\max}$. The horizontal dashed line is the average over these instantaneous values $\langle\theta_2(\gamma)\rangle$, while the horizontal solid line is θ_2 as obtained from averaging the orientational ordering tensor over the entire shearing run. The system has $N = 1024$ particles. (b) Fourier transform of $\theta_2(\gamma)$, $\mathcal{F}[\theta_2]$, vs dimensionless frequency $\omega/\dot{\gamma}$. The high frequency tail is fit to an inverse power law (dashed line) and gives an exponent ~ 1.5.

II. SPATIAL CORRELATIONS

Since our system has finite nematic orientational order, we wish to check whether there might also be smectic translational order, with particles flowing in well defined layers oriented in the direction of the flow. To test for this, we measure the following transverse correlation function of the particle center of mass density $n(\mathbf{r})$. We first define,

$$n(y) = \frac{1}{\Delta y \mathcal{L}_\perp^{d-1}} \int_{y-\Delta y/2}^{y+\Delta y/2} dy' \int_0^{\mathcal{L}_\perp} d\mathbf{r}_\perp\, n(y', \mathbf{r}_\perp). \quad \text{(SM-1)}$$

$n(y)$ is just he number of particles per unit volume whose center of mass lies in a layer of small width Δy that spans the system in the orthogonal directions. For $d = 2$ dimensions, $\mathbf{r}_\perp = x\hat{\mathbf{x}}$ and $\mathcal{L}_\perp = \mathcal{L}_x$, the length of the system in the $\hat{\mathbf{x}}$ direction; for $d = 3$, $\mathbf{r}_\perp = x\hat{\mathbf{x}} + z\hat{\mathbf{z}}$ and $\mathcal{L}_\perp = \mathcal{L}_x = \mathcal{L}_z$. We then define the correlation

$$C(y) = \frac{\mathcal{L}_\perp^{d-1}}{n\mathcal{L}_y} \int_0^{\mathcal{L}_y} dy' \left[\langle n(y+y')n(y')\rangle - \langle n\rangle^2\right], \quad \text{(SM-2)}$$

where the prefactor is chosen so that $C(y)$ is independent of the system size.

We consider first the case of spherocylinders in 2D, where we average over large total strains $\gamma \approx 130$, thus allowing for accurate measurements of $C(y)$. For our calculations we use a layer width $\Delta y = 0.01$ for $\alpha \leq 0.01$, and $\Delta y = 0.025$ for larger α. In Fig. SM-6a we plot $C(y)$ vs y for $\alpha = 0$, 0.001, and 0.01 at $\phi = 0.845$, which is just slightly above the jamming $\phi_J^{(0)} = 0.8433$ for circular disks. In each case we use the smallest $\dot{\gamma}$ we have simulated at each α, i.e. 10^{-6}, 4×10^{-7} and 4×10^{-7} respectively. We see that the $C(y)$ for these three cases are almost indistinguishable; there is nothing that signals

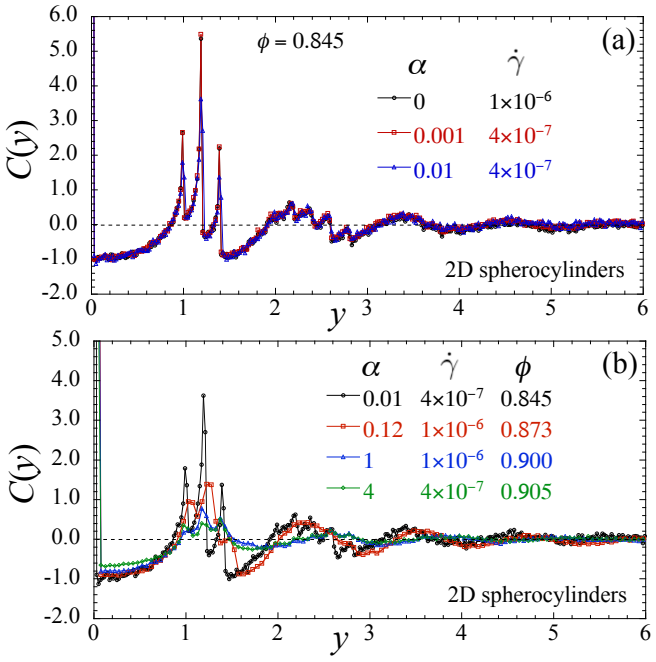

FIG. SM-6. Spatial correlations in the direction of the flow velocity gradient, $C(y)$ vs y, for 2D spherocylinders. (a) Results for small α, including $\alpha = 0$, at the common value of $\phi = 0.845$, just above the jamming fraction for circular disks, $\phi_J^{(0)} = 0.8433$; strain rates $\dot\gamma$ are as indicated in the figure. (b) Results for larger values of α, at low strain rates $\dot\gamma$, just above their respective jamming fractions $\phi_J(\alpha)$; values of $\dot\gamma$ and ϕ are indicated in the figure.

a singular behavior as $\alpha \to 0$. We see sharp peaks at $y = 1$, 1.2, and 1.4, which are the nearest neighbor separations for just contacting small-small, small-big, and big-big pairs. At larger y we see oscillations with a period of 1.2, the average spacing between contacting particles. However these oscillations clearly decay to zero as y increases, thus demonstrating that there is only short ranged order in the direction of the flow velocity gradient. Fitting the heights of the larger y peaks to an exponential, we find a decay length between 1 and 2.

In Fig. SM-6b we plot $C(y)$ vs y for larger values of α, at our lowest strain rate for each case, and at a packing fraction ϕ that is slightly above the respective jamming fraction ϕ_J for each α. We again see similar behavior: oscillations that decay to zero as y increases. As α increases, and the particles become increasingly nonspherical, the sharp peaks near $y = 1$, 1.2 and 1.4 broaden and the peaks at $y > 2$ shift to slightly larger values of y; results for $\alpha = 1$ and $\alpha = 4$ are nearly indistinguishable for $y > 2$. However the average spacing between peaks remains ~ 1.2 and the decay length remains in the range 1 to 2. We have verified that similar behavior occurs as either ϕ or $\dot\gamma$ is varied. We thus conclude that particles do not flow in well defined, spatially ordered, layers and so there is no smectic ordering.

Our 3D simulations are much more time consuming and we only shear to total strains $\gamma \approx 1.4$, thus greatly reducing the number of independent samples we have to average over when computing $C(y)$. To keep statistical accuracy reasonable, we therefore average over a thicker (as compared to 2D) layer of width $\Delta y = 0.18$ to define $n(y)$, so as to have more particles in the layer and so smaller fluctuations. Our results for the correlations of 3D ellipsoids are shown in Fig. SM-7. While the larger Δy means we lack the finer scale features seen in Fig. SM-6 for 2D, we continue to see similar decaying oscillations, characteristic of the absence of any long range translational ordering.

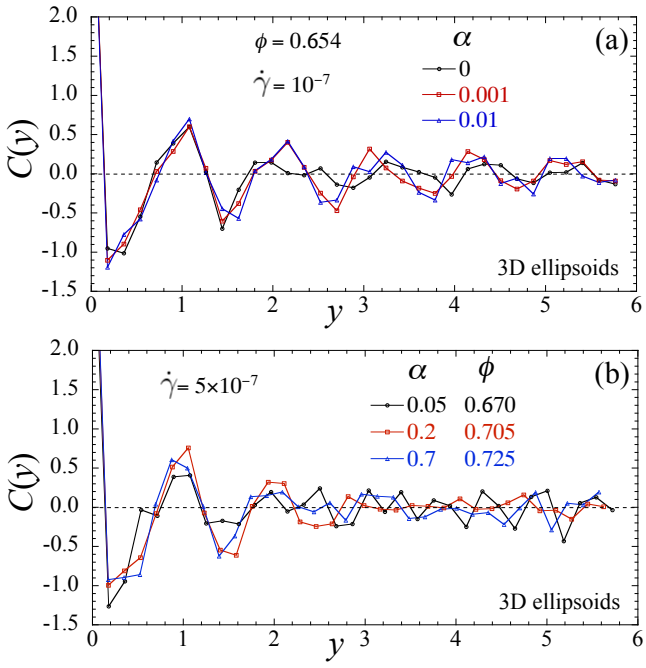

FIG. SM-7. Spatial correlations in the direction of the flow velocity gradient, $C(y)$ vs y, for 3D ellipsoids. (a) Results for small α, including $\alpha = 0$, at strain rate $\dot\gamma = 10^{-7}$ and the common value of $\phi = 0.654$, just above the jamming fraction for spheres, $\phi_J^{(0)} = 0.649$. (b) Results for larger values of α, at strain rates $\dot\gamma = 5 \times 10^{-7}$, just above their respective jamming fractions $\phi_J(\alpha)$; values of ϕ are indicated in the figure.

Note, since we use $N = 1024$ particles in both 2D and 3D, the system length for our 2D systems is $\mathcal{L} \sim 37$, while for 3D it is $\mathcal{L} \sim 11$. Thus in 3D the oscillations in $C(y)$ have not quite decayed to zero before one reaches $y = \mathcal{L}/2$, where the periodic boundaries influence our results and give a larger $C(y)$ than would be found in a larger system. Nevertheless our results in 3D are consistent with decaying correlations, and so the absence of any smectic ordering.

III. CONTACT LOCATION DISTRIBUTION

In the main text we showed in Fig. 5 that the probability density per unit surface area $\mathcal{P}(\vartheta)$, for a particle to

have a contact at polar angle ϑ on its surface, had a sharp peak at $\vartheta = \pi/2$, where the particle width is narrowest. The height of this peak increases as the asphericity α decreases. The results for $\mathcal{P}(\vartheta)$ vs ϑ shown in Fig. 5 were for a small strain rate $\dot\gamma$ at a fixed packing fraction near the jamming transition for spherical particles, $\phi \approx \phi_J^{(0)}$.

In Fig. SM-8 we plot the peak height $\mathcal{P}(\pi/2)$ vs packing ϕ at fixed small α, for different values of $\dot\gamma$. In (a) we show 2D spherocylinders at $\alpha = 0.03$ and in (b) 3D ellipsoids at $\alpha = 0.05$. We see that as $\dot\gamma$ decreases, $\mathcal{P}(\pi/2)$ increases to a limiting curve, which rises rapidly as ϕ approaches $\phi_J^{(0)}$, and then stays above the spherical particle value of unity as ϕ increases above the jamming transition. Thus the onset for the contacts to preferentially lie along the narrowest width of the particle takes place as ϕ passes through the jamming transition.

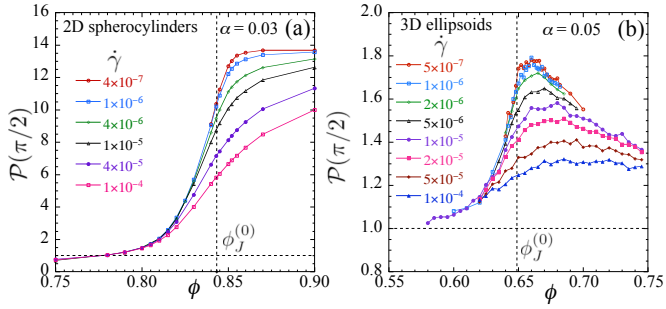

FIG. SM-8. Peak probability $\mathcal{P}(\pi/2)$ vs packing ϕ for different strain rates $\dot\gamma$ for (a) 2D spherocylinders at $\alpha = 0.03$ and (b) 3D ellipsoids at $\alpha = 0.05$. As $\dot\gamma$ decreases, the peak value $\mathcal{P}(\pi/2)$ increases until it saturates. Vertical dashed lines denote the jamming point of spherical particles $\phi_J^{(0)}$, while horizontal dashed lines indicate the value of unity expected for a spherical particle.

IV. RESPONSE TO A PURE SHEAR DEFORMATION

It is interesting to compare the response of our system to a pure, rather than a simple, shear. For simplicity we consider this for the case of our 2D spherocylinders. In this model the dissipative force is determined by the relative velocity of the particle with respect to an affinely deformed background host medium. We define the local velocity $\mathbf{v}_{\rm host}(\mathbf{r})$ of this background host in terms of a strain rate tensor $\dot{\mathbf{\Gamma}}$, i.e., $\mathbf{v}_{\rm host} = \dot{\mathbf{\Gamma}} \cdot \mathbf{r}$. A simple shear deformation can be decomposed into the sum of a pure shear and a uniform rotation,

$$\dot{\mathbf{\Gamma}}_{\rm ss} = \dot{\mathbf{\Gamma}}_{\rm ps} + \dot{\mathbf{\Gamma}}_{\rm rot}. \qquad \text{(SM-3)}$$

For our coordinate system with simple shear flow in the $\hat{\mathbf{x}}$ direction, this becomes,

$$\begin{bmatrix} 0 & \dot\gamma \\ 0 & 0 \end{bmatrix} = \begin{bmatrix} 0 & \dot\gamma/2 \\ \dot\gamma/2 & 0 \end{bmatrix} + \begin{bmatrix} 0 & \dot\gamma/2 \\ -\dot\gamma/2 & 0 \end{bmatrix}. \qquad \text{(SM-4)}$$

The first term on the right hand side is a pure shear, with expansion along the $(1,1)$ diagonal and compression along the $(1,-1)$ diagonal, both at the rate $\dot\gamma/2$ so as to keep the area constant. The second term is a clockwise rotation $(-\dot\gamma/2)\hat{\mathbf{z}} \times \mathbf{r}$, with angular velocity $-\dot\gamma/2$. It is this second term which drives the continuous rotation of particles under simple shear, resulting in the finite $-\langle\omega_{zi}\rangle/\dot\gamma > 0$ seen in Fig. 3 of the main text.

Under pure shear there is no such rotational drive, and particles try to relax from their initial orientation to one aligned with the expansive direction of the pure shear. Rotating coordinates so that the expansive direction is $\hat{\mathbf{x}}$ and the compressive direction is $\hat{\mathbf{y}}$, the rotational equation of motion for pure shear becomes,

$$\dot\theta_i = -(\dot\gamma/2)[\Delta I_i/I_i]\sin 2\theta_i + \tau_i^{\rm el}/(k_d v_i I_i). \qquad \text{(SM-5)}$$

For an isolated particle where $\tau_i^{\rm el} = 0$, particles will exponentially relax to $\theta_i = 0$ or π with a relaxation time t_0 set by the total strain $\gamma_0 = \dot\gamma t_0 = I_i/\Delta I_i$. Thus, at low ϕ near this isolated particle limit, we expect to find near perfect nematic ordering with $S_2 \approx 1$ and $\theta_2 = 0$. However, as the asphericity α of the particles vanishes, the relaxation time needed to achieve this highly ordered state diverges as $\dot\gamma t_0 = (I_i/\Delta I_i) \sim 1/\alpha$.

To investigate the response to pure shear at dense ϕ, we have carried out numerical simulations. A practical limitation of pure shear simulations is that, unlike for simple shear, there is a limit to the total strain γ that can be applied to a finite numerical system before the system collapses to a narrow height of order one particle width, $L_y(\gamma) = L_y(0)e^{-\gamma/2} \sim O(1)$. To increase the total possible strain γ, we use systems of $N = 1024$ particles with an initial system aspect ratio of $L_y(0)/L_x(0) = 8$, and shear to a strain γ such that $L_y(\gamma)/L_x(\gamma) = 1/8$, thus allowing a maximum strain of $\gamma = \ln 64 \approx 4.2$. We use a strain rate $\dot\gamma = 10^{-6}$, and average over four independently generated samples.

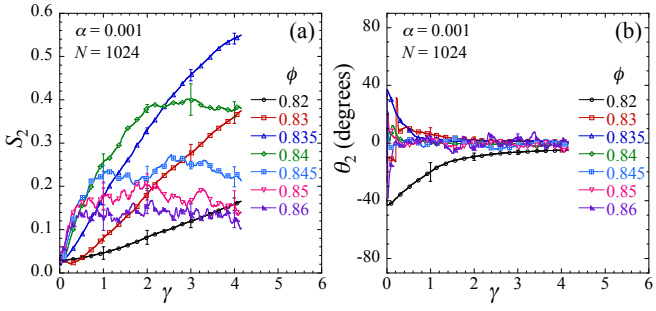

FIG. SM-9. (a) Magnitude S_2 and (b) direction θ_2 of the nematic order parameter vs pure strain $\gamma = \dot\gamma t$, at different packing fractions ϕ for nearly circular particles with $\alpha = 0.001$ at strain rate $\dot\gamma = 10^{-6}$. A sparse set of symbols is used to help differentiate curves of different ϕ, with many data points existing between adjacent symbols on any curve. Representative error bars are shown at integer values of γ.

Here we present results for nearly circular particles at

our smallest $\alpha = 0.001$. In Fig. SM-9 we plot the nematic order parameter magnitude S_2 and orientation θ_2 vs pure shear strain γ, for several different packing fractions ϕ. As γ increases, S_2 increases and θ_2 decays from its initial random value to zero, in agreement with the expectation that particles try to relax to their preferred orientation aligned with the expansive direction $\hat{\mathbf{x}}$. However we see that we are only able to reach the desired steady state, where S_2 plateaus to a constant value as γ increases, for relatively dense systems close to and above jamming, $\phi \geq 0.84$.

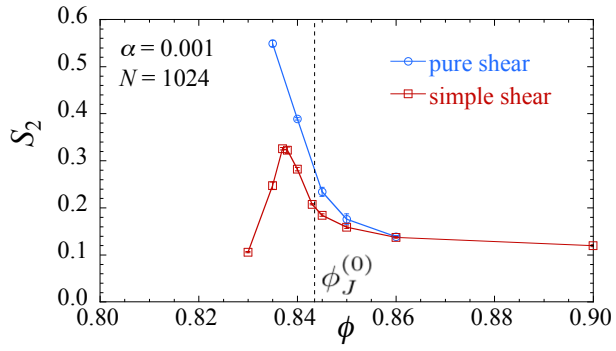

FIG. SM-10. Magnitude of the nematic order parameter S_2 vs packing ϕ, comparing pure shear with simple shear, for nearly circular particles with $\alpha = 0.001$. For pure shear the strain rate is $\dot{\gamma} = 10^{-6}$, while for simple shear $\dot{\gamma} = 10^{-7}$. Results represent steady state values, except for the pure shear case at $\phi = 0.835$ where steady-state has not quite been reached; the value shown at this ϕ is therefore a lower bound on the steady state limit.

In Fig. SM-10 we show the resulting steady state values of S_2 vs packing ϕ, comparing results from simple shear with those from pure shear. We see dramatically different behavior at low ϕ. For simple shear the nearly uniform rotation of the $\alpha = 0.001$ particles results in a small S_2, while for pure shear the relaxation to the expansive direction gives a large S_2. As ϕ increases, so does the rate of particle collisions. For pure shear the collisions and resulting excluded volume inhibit perfect alignment of particles and S_2 decreases. For simple shear the increasing collisions initially cause the rotation to slow (see Fig. 3a of the main text) and consequently S_2 to increase, but upon further increasing ϕ towards ϕ_J and going above, excluded volume effects similar to that in pure shear presumably inhibit alignment and cause S_2 to decrease, and we find that S_2 for both pure and simple shear become comparable and behave similarly. The non-monotonic behavior of S_2 in simple shear is thus a consequence of the rotational drive, present in simple shear but absent in pure shear. However in both simple and pure shear, we find that S_2 at jamming remains surprisingly large, even though the particles are extremely close to circular, with the flat sides of the spherocylinders comprising only a fraction $\alpha/(\alpha + \pi/2) = 6.4 \times 10^{-4}$ of the particle perimeter.

V. DETERMINATION OF CONTACTS AND OVERLAPS

In this section we summarize how we determine if two particles are overlapping, and if so, what is the point of contact between them. For our 2D spherocylinders, we use the efficient algorithm of Pournin et al. [1] to compute the shortest distance r_{ij} between the spines of two spherocylinders i and j. The line of length r_{ij} that connects the two spines we will call the line IJ. Whenever $r_{ij} < d_{ij} = (D_i + D_j)/2$, with D_i the diameter of the endcap of spherocylinder i, the two spherocylinders are overlapping. We then define the point of contact $\mathbf{r}_C$, at which the elastic force acts, as the distance $[D_i/(D_i + D_j)]r_{ij}$ from the spine of spherocylinder i, along the line IJ.

For our 3D ellipsoids, the procedure is more complicated. As illustrated in Fig. SM-11, for two overlapping ellipsoids i and j one can define a scale factor $\delta_{ij} < 1$ such that there exists a unique point of contact $\mathbf{r}_C$ between these ellipsoids when their axes are rescaled by the common factor δ_{ij}, keeping their center of mass positions fixed. This scale factor δ_{ij} can be computed using a method introduced by Perram and Wertheim (PW) [2] which has been applied to the study of jammed packings of ellipsoidal particles [3, 4]. Here we briefly summarize this method.

For any position $\mathbf{r}$, we define the scale function $\delta_i(\mathbf{r})$ such that $\mathbf{r}$ will lie on the surface of ellipsoid i if its axes are rescaled by $\delta_i(\mathbf{r})$. We then introduce the contact function $F(\mathbf{r}, \lambda)$ defined for two ellipsoids i and j,

$$F(\mathbf{r}, \lambda) = \lambda \delta_i^2(\mathbf{r}) + (1 - \lambda)\delta_j^2(\mathbf{r}), \tag{SM-6}$$

where $\lambda \in [0, 1]$. It has then been demonstrated [2] that there exists an $\mathbf{r}(\lambda)$ such that

$$\boldsymbol{\nabla} F(\mathbf{r}(\lambda), \lambda) = 0, \tag{SM-7}$$

where $\boldsymbol{\nabla} \equiv \partial/\partial \boldsymbol{r}$. This implies that

$$\lambda \boldsymbol{\nabla} \delta_i^2(\mathbf{r}(\lambda)) = -(1 - \lambda)\boldsymbol{\nabla} \delta_j^2(\mathbf{r}(\lambda)), \tag{SM-8}$$

which shows that when ellipsoids i and j are rescaled by factors $\delta_i(\mathbf{r}(\lambda))$ and $\delta_j(\mathbf{r}(\lambda))$ respectively, the point $\mathbf{r}(\lambda)$ lies on the surfaces of both ellipsoids, and the normal vectors to the surfaces at this point are parallel but pointing in opposite directions, so that the two ellipsoids are tangent at $\mathbf{r}(\lambda)$.

PW further showed [2] that $F(\mathbf{r}(\lambda), \lambda)$, as a function of $\lambda \in [0, 1]$, has a unique maximum at λ^*, such that

$$\begin{aligned} 0 &= \left.\frac{dF(\mathbf{r}(\lambda), \lambda)}{d\lambda}\right|_{\lambda=\lambda^*} \\ &= \left.\frac{\partial F(\mathbf{r}(\lambda), \lambda)}{\partial \lambda}\right|_{\lambda=\lambda^*} + \mathbf{r}(\lambda^*) \cdot \boldsymbol{\nabla} F(\mathbf{r}(\lambda^*), \lambda^*), \end{aligned} \tag{SM-9}$$

where the second term vanishes due to Eq. (SM-7). From Eq. (SM-6) we then find $\delta_i^2(\mathbf{r}(\lambda^*)) = \delta_j^2(\mathbf{r}(\lambda^*))$, which

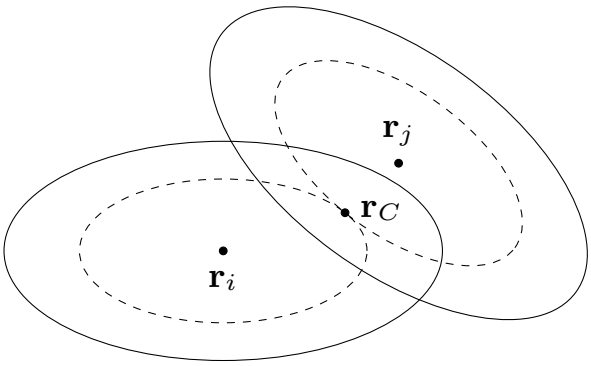

FIG. SM-11. Solid lines denote two overlapping ellipsoids i and j, with centers $\mathbf{r}_i$ and $\mathbf{r}_j$ respectively; the overlap is exaggerated over what is found in the actual simulations for the sake of clarity. Dashed lines show the same two ellipsoids when their axes are rescaled by a common factor δ_{ij}, so that they now have a single point of contact at $\mathbf{r}_C$.

means that the scale factor is the same for both ellipsoids, and

$$\delta_i^2(\mathbf{r}(\lambda^*)) = \delta_j^2(\mathbf{r}(\lambda^*)) = F(\mathbf{r}(\lambda^*), \lambda^*). \tag{SM-10}$$

The scale factor δ_{ij} that we are seeking is thus defined as

$$\delta_{ij}^2 = \max_{\lambda\in[0,1]} [F(\mathbf{r}(\lambda), \lambda)]. \tag{SM-11}$$

With this notation, we define the point of contact between ellipsoids i and j as $\mathbf{r}_C = \mathbf{r}(\lambda^*)$. It is thus the unique point common to ellipsoids i and j when both are rescaled with a common factor δ_{ij}.

To compute the scale factor δ_{ij} defined in Eq. (SM-11), we use a method derived from Ref. [4]. An ellipsoid i is defined by its center of mass position $\mathbf{r}_i$, the lengths of its axes (a_1, a_2, a_3), and the rotation matrix $\boldsymbol{\mathcal{Q}}_i$ that rotates the (x, y, z) directions of the lab coordinate frame onto the principal axes of the ellispoid. We then introduce the matrix,

$$\mathbf{B}_i = \boldsymbol{\mathcal{Q}}_i \cdot \begin{pmatrix} a_1^{-2} & 0 & 0 \\ 0 & a_2^{-2} & 0 \\ 0 & 0 & a_3^{-2} \end{pmatrix} \cdot \boldsymbol{\mathcal{Q}}_i^{-1}, \tag{SM-12}$$

which is symmetric due to the orthogonal nature of $\boldsymbol{\mathcal{Q}}_i$, and gives an explicit definition of the scale function $\delta_i(\mathbf{r})$,

$$\delta_i^2(\mathbf{r}) = (\mathbf{r} - \mathbf{r}_i) \cdot \mathbf{B}_i \cdot (\mathbf{r} - \mathbf{r}_i). \tag{SM-13}$$

Eq. (SM-8) then becomes

$$\lambda \mathbf{B}_i \cdot (\mathbf{r}(\lambda) - \mathbf{r}_i) = -(1-\lambda)\mathbf{B}_j \cdot (\mathbf{r}(\lambda) - \mathbf{r}_j). \tag{SM-14}$$

After introducing [2]

$$\mathbf{Y}_{ij}(\lambda) = \lambda \mathbf{B}_j^{-1} + (1-\lambda)\mathbf{B}_i^{-1},$$

and defining $\mathbf{r}_{ji} = \mathbf{r}_j - \mathbf{r}_i$, Eq. (SM-14) gives expressions for the distances between the contact point $\mathbf{r}(\lambda)$ and the centers of the ellipsoids,

$$\begin{aligned} \mathbf{r}(\lambda) - \mathbf{r}_i &= (1-\lambda)\mathbf{B}_i^{-1} \cdot \mathbf{Y}_{ij}^{-1}(\lambda) \cdot \mathbf{r}_{ji}, \\ \mathbf{r}(\lambda) - \mathbf{r}_j &= -\lambda \mathbf{B}_j^{-1} \cdot \mathbf{Y}_{ij}^{-1}(\lambda) \cdot \mathbf{r}_{ji}. \end{aligned} \tag{SM-15}$$

As discussed above, the unique contact point $\mathbf{r}_C$ for equal scale factors, $\delta_{ij} = \delta_i(\mathbf{r}_C) = \delta_j(\mathbf{r}_C)$, is found by maximizing the contact function $F(\mathbf{r}(\lambda), \lambda)$ with respect to λ. Using the above results and Eq. (SM-13) in Eq. (SM-6) thus gives,

$$\begin{aligned} F(\mathbf{r}(\lambda), \lambda) &= \lambda(1-\lambda)\mathbf{r}_{ji} \cdot \mathbf{Y}_{ij}^{-1}(\lambda) \cdot \mathbf{r}_{ji} \\ &= \frac{\lambda(1-\lambda)\mathbf{r}_{ji} \cdot \mathrm{adj}[\mathbf{Y}_{ij}(\lambda)] \cdot \mathbf{r}_{ji}}{\det[\mathbf{Y}_{ij}(\lambda)]} \\ &\equiv \frac{p_{ij}(\lambda)}{q_{ij}(\lambda)}, \end{aligned} \tag{SM-16}$$

where adj[...] denotes the adjugate matrix (whose element (α, β) is equal to the determinant of the 2×2 submatrix obtained after eliminating row β and column α from the original 3×3 matrix), and det[...] denotes the determinant. The functions $p_{ij}(\lambda)$ and $q_{ij}(\lambda)$ are polynomials in λ of degree 4 and 3 respectively.

The desired parameter λ^*, at which $F(\mathbf{r}(\lambda), \lambda)$ is maximized, is then the unique root in the interval $[0, 1]$ of the 6th degree polynomial

$$h_{ij}(\lambda) = p'_{ij}(\lambda) q_{ij}(\lambda) - p_{ij}(\lambda) q'_{ij}(\lambda), \tag{SM-17}$$

i.e., $h_{ij}(\lambda^*) = 0$, where primes above denote derivatives with respect to λ.

Finally, to determine ellipsoid elastic interactions, we investigate all pairs of ellipsoids whose center of mass separation $|\mathbf{r}_i - \mathbf{r}_j|$ is small enough that the ellipsoids might be overlapping. We then apply the above procedure to determine δ_{ij}. If the resulting $\delta_{ij} > 1$, then the pair of ellipsoids are in fact not overlapping and so have no interaction. If $\delta_{ij} \leq 1$, then the ellipsoids overlap and the point of contact is taken as $\mathbf{r}_C$.

[1] L. Pournin, M. Weber, M. Tsukahara, J.-A. Ferrez, M. Ramaioli, and T. M. Liebling, "Three-dimensional distinct element simulation of spherocylinder crystallization," Granul. Matter **7**, 119 (2005).

[2] J. W. Perram and M. Wertheim, "Statistical mechanics of hard ellipsoids. I. Overlap algorithm and the contact function," Journal of Computational Physics **58**, 409 (1985).

[3] A. Donev, R. Connelly, F. H. Stillinger, and S. Torquato, "Underconstrained jammed packings of nonspherical hard particles: Ellipses and ellipsoids," Phys. Rev. E **75**, 051304

(2007).
[4] A. Donev, "Jammed Packings of Hard Particles," Ph.D. thesis, Princeton University (2006), available from: http://cims.nyu.edu/~donev/Thesis.pdf